

Numerical Investigation of the Effect of Preexisting Discontinuities on Hydraulic Stimulation

Eleni Gerolymatou^{a,*}, Sergio-Andres Galindo-Torres^b, Theodoros Triantafyllidis^a

^a*Institute of Soil Mechanics and Rock Mechanics, Karlsruhe Institute of Technology,
Engler-Bunte-Ring 14, 76131 Karlsruhe*

^b*Geotechnical Engineering Centre/Research Group on Complex Processes in Geo-Systems,
The University of Queensland, Brisbane QLD 4072 Australia*

Abstract

The present work aims to investigate the effect of the orientation and spacing of preexisting planes of weakness (discontinuities) on the process of hydraulic stimulation. Structured assemblies of spheropolyhedra were created and a constant water inflow was applied at their center. The hydraulic pressure and the resulting fracture pattern were monitored during each simulation. Both showed a strong dependence on the geometry of the preexisting discontinuities and the orientation of the stress field. The dependence of the maximum hydraulic pressure in each simulation on the geometry of the preexisting discontinuities was found to be compatible with continuum considerations.

Keywords: Discrete Elements, hydraulic stimulation, spheropolyhedra, discontinuities, fracture orientation, fracture spacing

1. Introduction

The increasing demand for energy at the least possible environmental impact in the last years has led to an ever-increasing interest in geothermal energy world-wide. This kind of renewable, sustainable energy source has the advan-

*Corresponding author

Email addresses: eleni.gerolymatou@kit.edu (Eleni Gerolymatou),
s.galindotorres@uq.edu.au (Sergio-Andres Galindo-Torres),
theodoros.triantafyllidis@kit.edu (Theodoros Triantafyllidis)

tage of continuous supply, as opposed for example to solar or wind energy. Though the energy present in the form of heat in the upper crust is abundant, geothermal power is not. This stems from the fact that the required combination of elevated temperature and relatively high permeability does not exist everywhere. Most areas with elevated temperature gradients are hot but have a relatively low permeability. In such cases hydraulic stimulation is used to

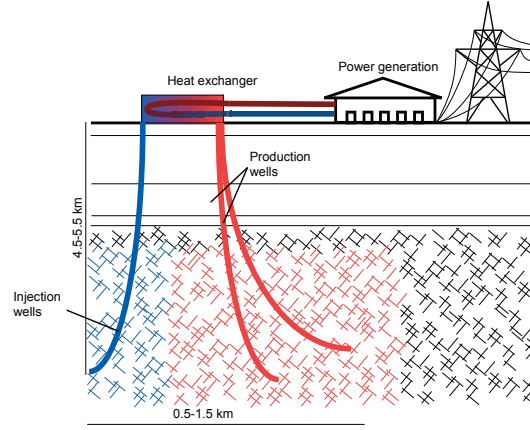


Figure 1: Reservoir outline.

increase permeability and thus reservoir productivity.

Though a lot of progress has been made in the direction of the simulation of hydraulic fracturing, the reservoir rock is usually viewed as a continuum without preferential directions as to the formation of the fractures [1, 2, 3]. The aim of the present work is to examine the problem of the hydraulic fracturing of a rock mass with pre-existing sets of discontinuities with given orientation and spacing. The schematic outline of the problem considered is exhibited in figure 1. In black are shown preexisting discontinuities that remain closed. The fractures through which flow takes place are denoted in blue and red, for colder and hotter water respectively.

As already mentioned, the present work is concerned with the hydraulic fracturing of a rock mass with pre-existing sets of discontinuities with given orientation and spacing. Such formations are often found in rock mass joints



(a) Orthogonal cross joints in a carbonate bed of the Monterey Formation, California, after Bai et. al. [4].



(b) Vertical aerial view showing joints in the flat-lying Cedar Mesa Sandstone, Utah, after Suppe [5].

Figure 2: Jointed rock mass.

and are a result of the preloading history of the formation. Two examples of
 25 unusually regular geometry are shown in figure 2. Figure 2a shows nearly rectangular blocks with significantly larger width than their height, while in figure 2b
 rhombic blocks with a side ratio of about one are to be seen. Within the frame
 of this work discrete element simulations of hydraulic fracturing of relatively
 simple assemblies of polyhedra were performed. The aim of this rather simple
 30 procedure is to elucidate the basic mechanisms involved in the flow stimulation
 in fractured media. The presence of load implies that fractures and discontinuities
 are to remain closed in the absence of fluid pressure. In the presence
 of high enough fluid pressure on the other hand, it is expected that the flow
 will eventually settle into preferential paths offering the least resistance. The
 35 simplicity of the approach renders it easy to modify parameters of the problem
 one at a time, such as discontinuity orientations and polyhedra geometry, but
 does by no means allow for quantitative conclusions. It is however expected that
 the results will contribute to the insight into the governing mechanisms of the
 examined process and thus prove a valuable help in the effort for a physically
 40 based modeling.

The application of the Discrete Element Method to the problem of hydraulic
 fracturing is not new. In the majority of the available works, as for example in

[6, 7, 8], disks or spheres are used in the simulations, though works with polygons are also available [9, 10]. Of particular interest is the work by Hamidi et. al. [11] who used a tetrahedral mesh and a highly compressible fracturing fluid to simulate the process. This work goes one step further by taking more general meshes and an fracturing fluid with a realistic compressibility. The cohesive bonds between the particles then break under the influence of the increase fluid pressure, to form fractures. Different geometries have been investigated with the above methodology. Eshiet et al. [6] considered rectangular specimens, consisting of disks, while Sousani et al. [8] considered hollow cylinder specimens consisting of spheres. Other numerical methodologies used to simulate the fracture evolution during hydraulic fracturing are extended Finite Element methods, such as Finite Elements incorporating discrete fractures and based on stress intensity factors for the fracture propagation [12], or the combined Finite-Discrete Element Method (FDEM)[13]. As the goal of the present work is to investigate the effect of the preexisting structure on the procedure of hydraulic fracturing or stimulation, polyhedra are used in our case. In many respects the present work is a continuation of the work of Galindo Torres et al. [14]. To the best knowledge of the authors, a study of structured assemblies in this context has not been performed before.

In the second section the numerical method used is described, while in the third the assumptions made are introduced. The results are presented and discussed in the fourth section, while in the fifth section conclusions are drawn.

2. Numerical Method

The code used in the present work was based on MechSys [15]. Mechsys is an open source library which runs in linux systems, and therefore, unlike the popular ITASCA software is free and can run in supercomputing clusters. Furthermore, the Mechsys DEM module offers a more general collision law based on the spheropolyhedra method which works when the particles are bonded together and when they are not. It can also model non-convex shapes ([16]),

particles obtained from Voronoi tessellations ([17]) and it has even been coupled, and extensively validated, with fluid dynamics simulation algorithms as shown in [18], or without as shown in [19].

75 A spheropolyhedron is a polyhedron that has been eroded and then dilated by a sphere element as seen in figure 3. The result is a body with similar dimensions but with rounded corners. The most important advantage of the

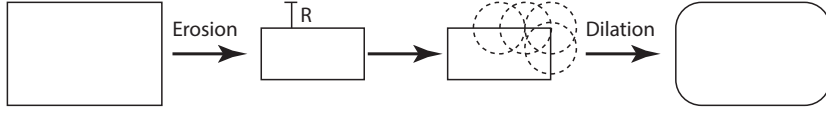


Figure 3: Polygon erosion and dilation.

spheropolyhedra technique is that it allows a straight-forward definition of the contact laws between the particles, due to the resulting smoothing of the edges.

80 In the spheropolyhedra approach a particle is defined as a set of vertices, edges and faces, where each geometrical feature is dilated by a sphere. For simplicity let the set of all geometric features of a particle P_k be denoted by $\{\mathcal{G}_k^i\}$. This means that the distance between two geometric features of the particles (1) and (2) is the minimum distance of two points belonging to them:

$$\text{dist}(\mathcal{G}_1^i, \mathcal{G}_2^j) = \min \left(\text{dist}(\vec{X}_i^{(1)}, \vec{X}_j^{(2)}) \right) \quad (1)$$

85 where $\vec{X}_i^{(k)}$ is a vector belonging to the set \mathcal{G}_k^i . Assuming the minimum distance for the sets \mathcal{G}_1 and \mathcal{G}_2 to be given by the Euclidean distance between two of their points \vec{X}_1 and \vec{X}_2 , the normal vector of the contact is defined as

$$\vec{n}(\mathcal{G}_1, \mathcal{G}_2) = \frac{\vec{X}_2 - \vec{X}_1}{\|\vec{X}_2 - \vec{X}_1\|} \quad (2)$$

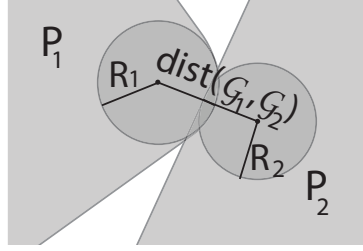
The normal contact force \vec{F}_n between these two features is defined as

$$\vec{F}_n(\mathcal{G}_1, \mathcal{G}_2) = K_n \delta(\mathcal{G}_1, \mathcal{G}_2) \vec{n}(\mathcal{G}_1, \mathcal{G}_2) \quad (3)$$

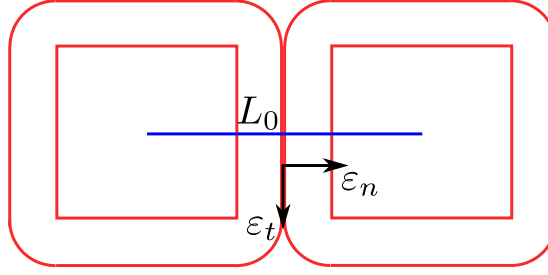
where K_n is a parameter called the normal stiffness and

$$\delta = \text{dist}(\mathcal{G}_1, \mathcal{G}_2) - R_1 - R_2 \quad (4)$$

⁹⁰ R_1 and R_2 being the spheroradii of the particles P_1 and P_2 respectively, as shown in figure 4a. The previous normal force is defined for a pair of geometric



(a) Definition of distance between two features



(b) Definition of the bonding force

Figure 4: Contact features.

features. The net elastic force is the addition of all the forces for each possible pair of geometric features.

Correspondingly, the tangential forces are defined in accordance with the
⁹⁵ Cundall-Strack spring method [20] as follows

$$\vec{F}_t = K_t \vec{\xi} \quad (5)$$

where K_t is the tangential stiffness and $\vec{\xi}$ is the incremental tangential displacement, whose increment is defined as

$$d\vec{\xi} = \vec{v}_t dt \quad (6)$$

In the above dt is the time step, \vec{v} is the relative velocity of the geometric features at the point of contact and \vec{v}_t is the component of \vec{v} that is tangential

100 to the normal vector. When $F_t > \mu F_n$, where μ is the friction coefficient, the force becomes $\vec{F}_t = \mu F_n \vec{\xi} / \xi$, where $\xi = \|\vec{\xi}\|$. As a result of particle rotations, $\vec{\xi}$ may not be perpendicular to the normal vector at any given time step. To rectify this, at each instant the normal component $(\vec{n} \cdot \vec{\xi})$ is subtracted from $\vec{\xi}$, as indicated in previous studies [21].

105 An additional, viscous, force is introduced for the stability of the simulation as follows:

$$\vec{F}_v = G_n m_e \vec{v}_n + G_t m_e \vec{v}_t \quad (7)$$

in which G_n and G_t are the normal and tangential viscous coefficients respectively, \vec{v}_n and \vec{v}_t the normal and tangential components of the relative velocity and m_e is the reduced mass of the particles in contact.

110 To model cohesion an elastic force is introduced between two adjacent spheropolyhedra sharing a common face as seen in figure 4b. The expression for the proposed bonding force in the normal direction is given by

$$\vec{F}_n^c = B_n A R(\varepsilon_n) \vec{n} \quad (8)$$

where B_n is the normal elastic modulus at the point of contact, A is the shared face area, ε_n is the normal strain (relative to the reference length L_0 of figure 4b) and \vec{n} is the surface unit normal vector of the shared face. The function $R(x)$ is the ramp function,

$$R(x) = \begin{cases} -x & \text{if } x < 0 \\ 0 & \text{otherwise} \end{cases} \quad (9)$$

thus ensuring that this force only opposes tensile displacements. A similar force is introduced for the tangential direction as

$$\vec{F}_t^c = B_t A \varepsilon_t \vec{t} \quad (10)$$

where \vec{t} is the vector tangential to the common face, ε_t is the tangential strain as a percentage of the reference length L_0 and B_t is the tangential elastic modulus. These two forces oppose both normal and tangential displacements. There is no need of other torques since the geometry itself prevent any further rotation

thanks to the interaction between corners in the spheropolyhedra approach.

To model fracture these forces must have a threshold value after which they
 125 cease to exist. In the present case the following debonding condition is used:

$$\frac{|\varepsilon_n| + |\varepsilon_t|}{\epsilon_{th}} > 1 \quad (11)$$

which is a modified version of the von Mises yield criterion commonly used in the beam model [22, 23, 24] with a given threshold ϵ_{th} which can be deduced from the tensile strength as explained in [25].

Finally all these forces are added to obtain the net force over a particle.
 130 Subsequently Newton's second law is numerically integrated as well as the Euler equations for the rotation of the bodies with the leap-frog algorithm.

For the generation of the particles, MechSys incorporates a mesh generator based on the Voronoi construction method. This was however unsuitable for the construction of the structured arrays necessary within the frame of this work.
 135 Therefore a suitable mesh generator was implemented, as explained below. Input parameters are the size of the domain, the approximate number of particles, the length to height ratio (aspect ratio dx/dy) and the inclination angles α and β , as shown in figure 5. The convention for the signs of α and β has been selected in this manner, so that blocks with $\alpha + \beta = 0$ are rectangular, but rotated in the clockwise direction by α . By modifying the above parameters different

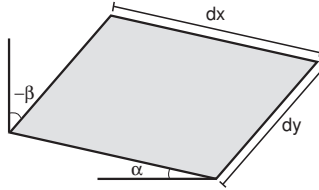


Figure 5: Example of a block's geometry.

140 assemblies of blocks resembling the structures shown in figure 2 are generated. Initially a much larger structured assembly is generated, which is then cropped to the appropriated size and shape for the final domain. The size of the initial assembly depends on the quantities α , β and dx/dy and was selected so as

145 to result in a final assembly of at least 1000 particles. The edge particles are suitably modified to maintain the same number of sides (quadrilaterals).

3. Assumptions

In this section the simplifying assumptions made for the numerical simulations are discussed. Though in reality the problem of hydraulic stimulation is three dimensional, in the present work the analysis was restricted to two dimensions for the sake of simplicity. Initially the horizontal and vertical loads were applied and the assembly was allowed to reach static equilibrium. Subsequently a constant inflow rate was imposed in the centre of the assembly and the ensuing pressure monitored, until the resulting fracture reached the boundary of the assembly. It is assumed that the hydraulic pressure is instantly applied on all fractured surfaces. The shear forces due to the flow of water are neglected. The applied boundary conditions are shown in figure 6. In the rest of this sec-

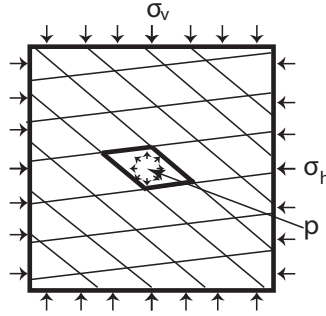


Figure 6: Applied boundary conditions.

tion the boundary conditions, the solid-fluid interaction and the test setup and preprocessing are discussed.

160 3.1. Boundary conditions

The boundaries are stress controlled. The stresses are applied by means of four rigid walls. In the third direction the displacements are constrained. The boundary stresses were selected on the basis of the *in situ* stress at the well

documented test site Soultz-sous-Forêts [26]. Those are of the order of tenths
165 of MPa [27]. In this work the vertical stress profile is estimated as

$$\sigma_v = -1.30 + 25.5z[km] \text{ MPa} \quad (12)$$

where z is the depth. The upper limit for the maximum principal stress is estimated as 1.21 σ_v , while the minimum principal stress is estimated as

$$\sigma_{h,min} = -1.78 + 14.06z[km] \text{ MPa} \quad (13)$$

These values provide an order of magnitude for the boundary stresses of the simulations, which will consequently be assumed to be of the order of tenths of
170 MPa, as already mentioned. In the following simulations the horizontal stress is set equal to 30 MPa and the vertical stress is set equal to 50 MPa.

3.2. Pressure as a function of fracture volume

In this section a simple analytical relationship correlating the pressure to the inflow of water and to the progress of the fracturing is derived. To this end
175 it is assumed that water pressure throughout the reservoir is spatially constant and all shearing effects due to water flow are ignored.

The common assumption of water incompressibility is raised, i.e. water is considered compressible. It results then that

$$p = p_0 + K\epsilon_v \quad (14)$$

where p is the pressure at time t , p_0 is the initial pressure, K is the bulk modulus
180 of water and ϵ_v is the volumetric strain of the water. The density that water has at the beginning of the procedure in the reservoir, though a constant in space by assumption, is not necessarily a constant in time. Under the assumption of absence of losses, mass must be conserved, meaning that the initial mass m_0 is equal to the final mass m_f

$$m_0 = m_f \Rightarrow \quad (15)$$

$$\rho_0 (Qt + V_0) = \rho_f (V_f) \Rightarrow \quad (16)$$

where Q is the injection rate, t is the time, V_0 is the initial reservoir volume, V_f is the current reservoir volume (initial volume plus the volume of the generated fractures), ρ_0 is the initial and ρ_f is the current water density in the reservoir.

The volumetric strain is defined as

$$\epsilon_V = \frac{V_{in} - V_{fin}}{V_{in}} = 1 - \frac{V_{fin}}{V_{in}} \quad (17)$$

190 where V_{in} is the initial water volume and V_{fin} is the final water volume. From the expression derived from the conservation of mass

$$\epsilon_V = 1 - \frac{V_f}{Qt + V_0} = \frac{Qt + V_0 - V_f}{Qt + V_0} \quad (18)$$

The effect of depth has been ignored in the current analysis. Its influence is introduced by means of the initial pressure p_0 .

The bulk modulus of water depends on pressure and temperature. Assuming
195 a reservoir temperature of about 93°C, the bulk modulus of water for different pressures is given in Table 1 [28]. The corresponding graph is shown in figure

p [MPa]	K [GPa]
0.1	2.30
10.3	2.36
31.0	2.50
103.4	2.94

Table 1: Bulk modulus of water as a function of pressure.

7 with a linear fitting. It is seen that the dependence is in good approximation linear. The expression for the pressure now becomes

$$p = p_0 + (K + K_0 \cdot p)\epsilon_V \quad (19)$$

with

$$K = 2.30 \text{ GPa}, \quad K_0 = 6.21 \quad (20)$$

200 if the pressure is expressed in GPa. Solving for the pressure yields

$$p = \frac{(p_0 + K)(Qt + V_0) - KV_f}{(1 - K_0)(Qt + V_0) + K_0V_f} \quad (21)$$

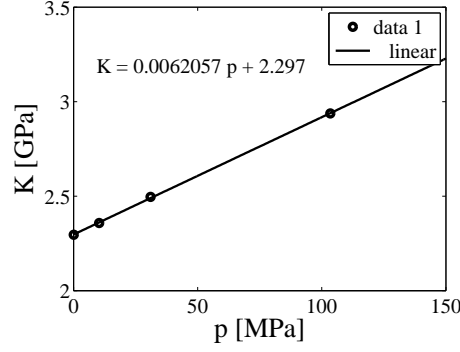


Figure 7: Dependence of water bulk modulus on pressure.

where equation (18) has been used.

The volume of the fractures is considered to be equal to the total change of volume in the assembly. While this is not accurate, there is no doubt that the fracture volume and the change in the volume of the whole assembly are closely
205 connected. It is further assumed that upon creation or propagation of a crack the hydraulic pressure is instantaneously applied on the newly formed surfaces as well.

3.3. Preprocessing and test set up

The parameters used for the simulations are summarized in Table 2. These

Contact stiffness, normal	10 GN/m
Contact stiffness, tangential	10 GN/m
Normal viscous coefficient	0.8 1/s
Tangential viscous coefficient	0.0 1/s
Tensile strength	10 MPa
Tangential Cohesion	10 MPa
Friction coefficient	0.8

Table 2: Parameters used in the simulations.

210 values were selected heuristically. As the obtained results are to be interpreted

only from a qualitative point of view, this is not expected to pose a problem. However the range of values taken lay within a realistic range as shown in [25]. The domain considered was square, with a side length of 500 m. Each assembly contains about 1000 blocks. The side ratio and the angles of the blocks vary,
215 but the surface of each block is maintained constant.

The *in situ* stresses are initially applied and the specimen is allowed to relax, i.e. static equilibrium is achieved. After the relaxation phase a constant inflow rate at the center of the assembly is applied (see figure 6). This was selected equal to $Q = 0.1 \text{ m}^3/\text{s}$ per meter. The initial hydraulic pressure was set equal
220 to the smallest principal stress, namely 30 MPa.

4. Results

In the present section the results of the simulations are presented. A total of 32 simulations were performed, each with about 1000 blocks, and with a different set of parameters α , β and dx/dy , shown in figure 5. From each
225 simulation the hydraulic pressure as a function of time and the pattern of the fracture were retrieved. In figure 8 the hydraulic pressure as a function of time

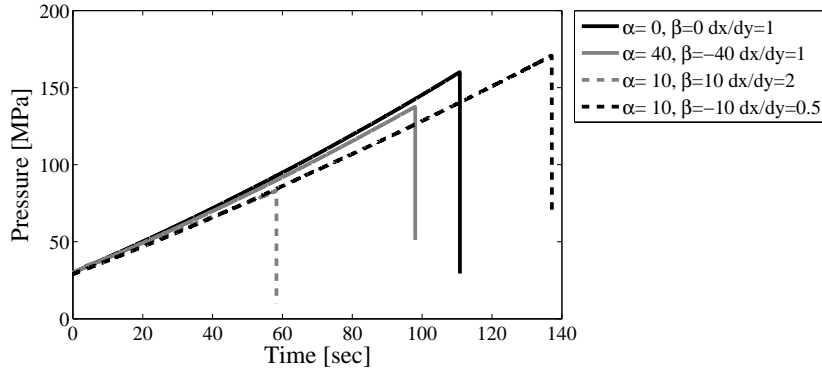


Figure 8: Pressure versus time for selected different geometries.

is given for different geometries. As may be seen, the geometry has a significant influence over the hydraulic pressure required to achieve fracture initiation and propagation, as well as on the time to fracture initiation. This is evidenced in

the varying values of maximum hydraulic pressure observed. The similar slope of the curves is obviously a result of the identical initial void volume for all assemblies. The rest of this section is subdivided into two subsections. In the first the effect of the geometry on the orientation of the fractures is presented. In the second subsection the influence of the geometry on the maximum hydraulic pressure is examined and the results are qualitatively compared with the analytical expressions for a single fracture in a continuum.

4.1. Geometry of fracture propagation

As already mentioned, in this subsection the dependence of the geometry of the ensuing fracture on the geometry of the blocks is examined. The evolution

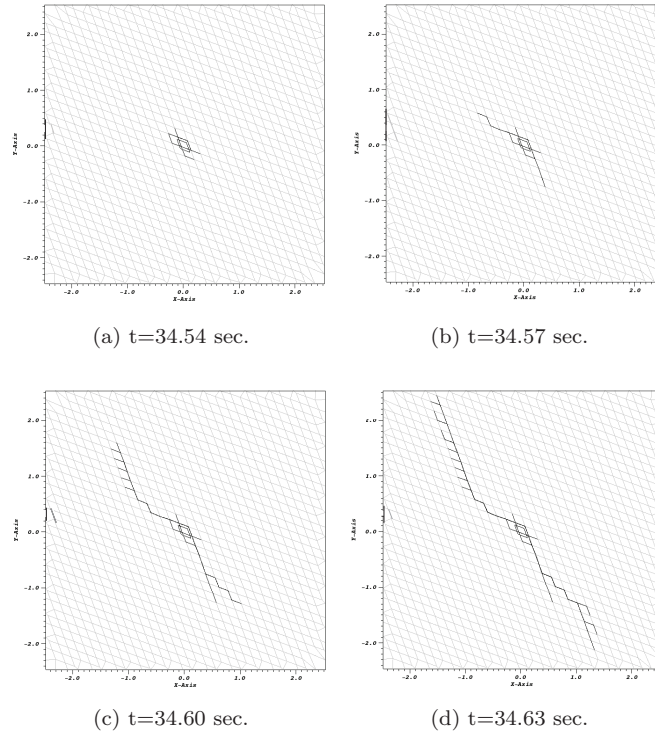


Figure 9: Fracture propagation for $\alpha = 20^\circ$, $\beta = 20^\circ$, $dx/dy=1$.

of the fracture for a specimen with $\alpha = 20^\circ$, $\beta = 20^\circ$ and $dx/dy=1$ (see figure

5) is shown in figure 9. As may be seen, the time to fracture initiation is about 34 sec, while the time required for the fracture to reach the boundary is about two orders of magnitude smaller.

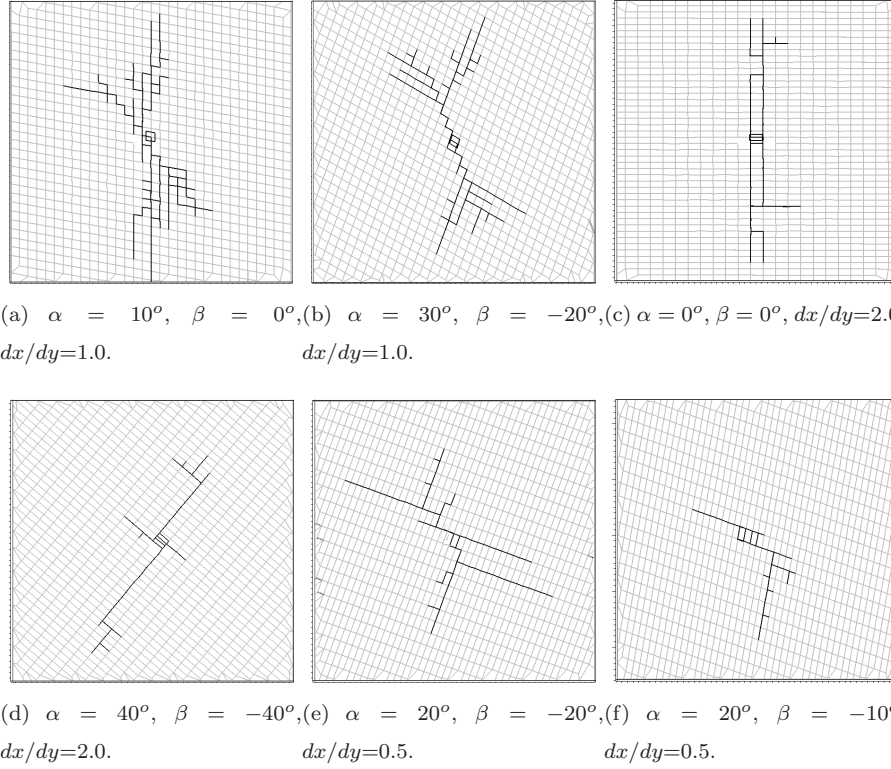


Figure 10: Fracture orientations.

In figure 10 the fractures resulting for a variety of different geometries are shown. Comparing figures 9d and 10a to figure 10f one may observe two different mechanisms of failure. Specimens with vertical or close to vertical discontinuities exhibit a crack that is normal to the direction of the minimum principal stress, which is in this case horizontal. Such behavior is shown in figure 10c and in part in figures 10a and 10f and is characteristic of tensile failure. In most cases however the failure mechanism is to be attributed to shear, or at least tension enhanced shear, as may be observed in figure 9d. This behavior is a direct result

of the anisotropy of the stress field. Particularly interesting is figure 10a, where two fractures may be observed, a vertical one, due to tensile failure, and an inclined one, due to shear.

255 The orientation of the preexisting discontinuities has a clear effect on the orientation of the resulting fractures. Another factor influencing this orientation is the spacing of these discontinuity planes. This is especially clear to see in figures 10e and 10f. While the preferential direction for tensile failure is the vertical one and the preferential direction for tensile failure is expected to form
 260 an angle of more than 60° to the horizontal, there are in both cases fractures with a much smaller inclination. This is to be attributed to the fact, that the length of the block sides in this direction is much smaller. The spacing of preexisting discontinuities may thus affect the direction of the hydraulic fractures, as well as the pressure required to achieve fracturing.

265 4.2. Maximum hydraulic pressure

In this section the dependence of the maximum hydraulic pressure observed in each simulation is examined as a function of the ratio dx/dy and the angles α and β , as shown in figure 5. Three families of samples were tested, with length ratios dx/dy of 0.5, 1.0 and 2.0 respectively. Within each family the
 270 angles α and β were varied. Plotting the maximum hydraulic pressure against the angles α and β yielded no clear correlation. The correlation to the sum of the angles was checked next. The results are shown in figure 11, where the black circles correspond to the side ratio of 1.0, open squares to 2.0 and gray diamonds to 0.5. As may be observed, the maximum pressure becomes smaller
 275 with increasing $\alpha + \beta$, that is, with increasing deviation of the shape of the blocks from the rectangular. This fact may be better understood by considering an averaged crack as in figure 12. The tortuosity of the resulting crack decreases with increasing $\alpha + \beta$ and the length of the averaged crack is analogous to

$$l_{eff} = \sqrt{d_x^2 + d_y^2 + 2d_x d_y \sin(\alpha + \beta)}. \quad (22)$$

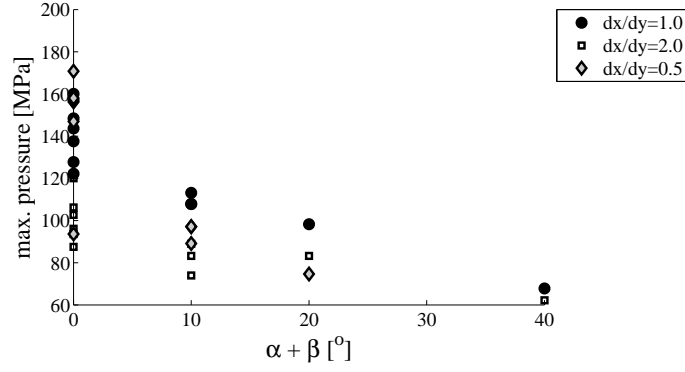


Figure 11: Pressure versus block geometry.

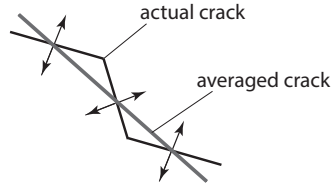


Figure 12: Water pressure in a crack.

The stress at the crack tip at failure is given on first approximation by

$$\sigma = A \frac{K_c}{l_{eff}} \quad (23)$$

280 according to Linear Elastic Fracture Mechanics, where A is a constant and K_c is the critical stress intensity factor. The above relation is shown qualitatively in figure 13. The resemblance to the numerical results in figure 11 is striking.

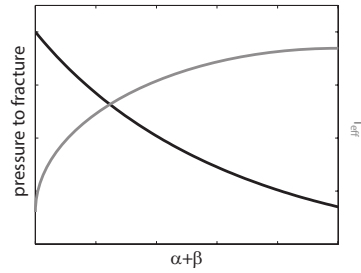


Figure 13: Pressure required for crack propagation based on stress intensity and corresponding length of the averaged crack.

It may thus be concluded that the reduction in the pressure required to achieve fracturing with increasing $\alpha + \beta$ is a result of the increase of the effective length of the fracture, or, equivalently, a result of the reduction of the tortuosity of the ensuing crack. The effect of the different side lengths of the blocks and the orientations accounts for the scattering observed, when comparing figure 11 to figure 13.

Subsequently the results for the specimens with fixed $\alpha + \beta = 0$ were plotted as a function of β and are shown in figure 14. The black circles correspond

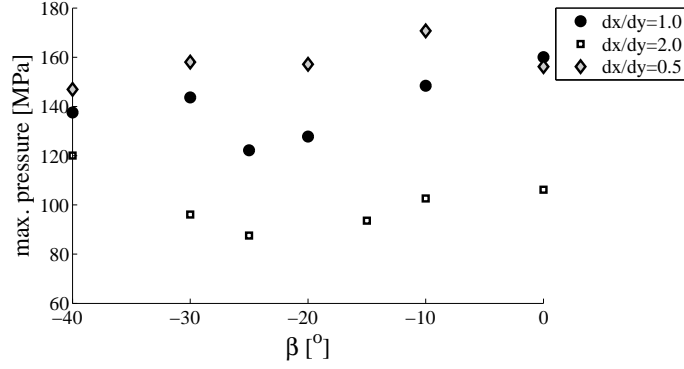


Figure 14: Pressure versus angle β .

to the side ratio of 1.0, open squares to 2.0 and gray diamonds to 0.5. $\beta = 0$ corresponds to vertical sides of the block, i.e. vertical preexisting discontinuities. It may be observed that the dependence on the angle β is similar for all three examined values of dx/dy , though the values of the maximum pressure are different. It is here attempted to pinpoint the mechanism leading to this behavior. Since fracture of the blocks is not possible, the failure must take place along these preexisting planes. For tensile failure to take place, it should hold that

$$p = \sigma_n - \sigma_t \quad (24)$$

where p is the pore pressure, σ_n the normal stress on the fracture and σ_t the tensile strength. For shear failure to take place, it should hold that

$$(\sigma_1 - p)(\sin(2\beta - \phi) - \sin(\phi)) = (\sigma_3 - p)(\sin(2\beta - \phi) + \sin(\phi)) + 2c \cos(\phi) \quad (25)$$

or, solving for the water pressure,

$$p = \frac{\sigma_1 + \sigma_3}{2} - \frac{\sigma_1 - \sigma_3}{2} \frac{\sin(2\beta - \phi)}{\sin(\phi)} + c \frac{\cos(\phi)}{\sin(\phi)} \quad (26)$$

where ϕ is the friction angle, σ_1 the maximum principal stress and the whole is based on the hypothesis of the validity of the Mohr-Coulomb failure criterion. The qualitative result is shown in figure 15. In reality both shear and tensile

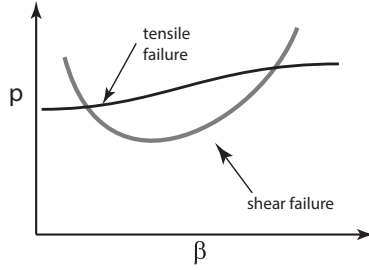


Figure 15: Theoretical mode and pressure of fracture propagation as a function of fracture orientation.

failure are present in almost all specimens. The dominant mechanism for each specimen is however in agreement with figure 15. An example is to be found in figure 16. It should be remarked that a modification of the tensile and shear strength of the bonds would certainly change the qualitative behavior of the bonds. In the extreme, it would be possible to suppress completely shear failure for example. The minimum of the hydraulic pressure in figure 14 is observed between absolute values of 20° and 30° , as would be expected from the theory, namely

$$\beta_0 = 90^\circ - \left(45^\circ + \frac{\phi}{2}\right) = 90^\circ - 64.33^\circ = 25.67^\circ \quad (27)$$

where ϕ is the friction angle. Moreover, tensile failure is bound to take place normal to the minimum stress, in this case in the vertical direction, and the

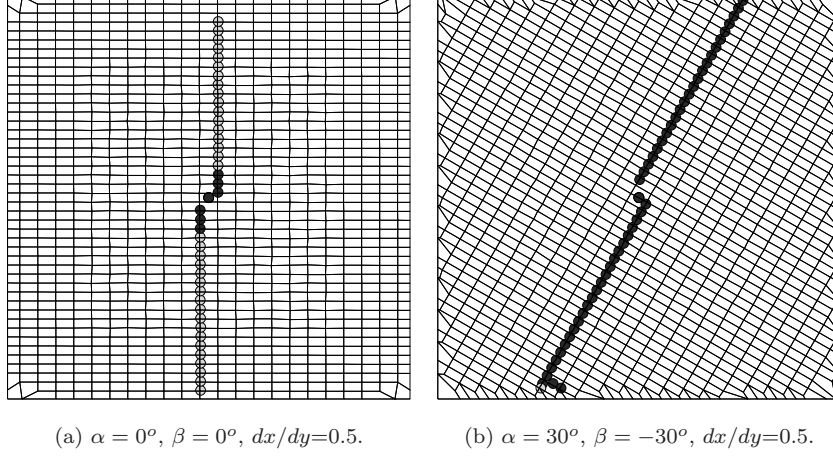


Figure 16: Modes of failure, shear in black and tensile in grey.

315 shear failure has a preferential direction closer to vertical than to the horizontal. As a result, it is to be expected that dy will have a stronger influence on the maximum hydraulic pressure than dx . In fact the pressure required to achieve fracture increases as dy increases, that is, as the discontinuities become less frequent in this direction, as shown by the results of figure 14. It is observed that
 320 assemblies with $dx/dy=2.0$, that is small spacing in the near vertical direction, require much smaller hydraulic pressures to fracture formation than assemblies with $dx/dy=0.5$, that is large spacing in the near vertical direction.

It may be concluded that the main influences detected are the block shape and orientation of the most favorably for shearing oriented discontinuity set. By
 325 this the discontinuity set whose orientation is closest to $\pi/4 + \phi/2$ (see equation (27)) with respect to the plane on which the maximum principal stress is acting is meant. These dependencies may in addition be explained and described with the aid of simple mechanical considerations.

5. Conclusions

330 In the present work the effect of preexisting sets of discontinuities on hydraulic fracturing was investigated, by means of discrete element simulations.

Structured spheropolyhedra assemblies were generated and a parametric analysis was performed. The parameters investigated were the orientation and spacing of the preexisting discontinuities. On the basis of the simulations performed, it is verified that both play a significant role in the process of hydraulic fracturing. The simulations, although not in a position to offer quantitative results, imply also that there is a dependence of the stimulation mechanism, i.e. shearing, tension and mixed modes, on the relative orientation of the discontinuities to the principal axes of the stress state. An interesting discussion on the subject of stimulation mechanisms may be found in [29].

It was observed that the orientation of the resulting fractures usually coincided with the direction most favorable to shear failure, evaluated in equation (27), as may be seen also in figure 10. Variations were observed in some special cases. Thus, when vertical fractures were present, cracks normal to the minimum in situ pressure formed in addition to the ones mentioned above. The only case in which no fracture formation in the least shear resistance direction was observed, were assemblies characterized by horizontal and vertical discontinuities. Apart from the discontinuity orientation, a marked effect of spacing was observed. In some of the simulations fractures formed also in the direction in which the discontinuity spacing was smaller, even though the orientation of the stress field was not favourable, as seen for example in figures 10e and 10f. It is worth remarking that these fractures were in any case formed in addition to the ones orientated favourably for fracture formation to the stress field. On the whole, in the vast majority of cases, the induced fractures where formed solely or at least also in the direction of least shear resistance, determined by the stress field imposed.

The value of the maximum hydraulic pressure observed in each numerical simulation was investigated as well. As was to be expected, it exhibited a strong dependence on the geometry of the preexisting discontinuities. Two geometric factors were found to play the most significant role. The first of these was the shape of the blocks, or otherwise, the angle between the two discontinuity families. For rectangular blocks larger values of the maximum hydraulic pressure

were observed. As the shape of the blocks became more and more removed from the rectangular, the maximum hydraulic pressure was found to decrease. This behavior was found to be qualitatively very similar to that of a tortuous crack that is averaged over its length, as far as its inclination is concerned. The side ratio of the blocks, or otherwise the discontinuity spacing, had an influence that was strongly dependent on the inclination of the discontinuities, as seen in figure 14.

The second geometric factor found to have a significant influence on the maximum value of the hydraulic pressure was the discontinuity inclination. To isolate this effect, the results for rectangular blocks only were plotted. The dependence was found to be qualitatively similar to the effect of a single fracture in a continuum according to classical rock mechanics. The effect of the spacing of the discontinuities was in this case clearly visible. The densest the spacing of the discontinuities in the direction of dy , the smaller the hydraulic pressure required to achieve fracturing. This was to be expected, as the smallest principal stress is the horizontal one. For all three spacings the dependence on the angle was however similar.

On the whole, it was found that the dependence of the pressure required to cause fracturing on the geometry of preexisting discontinuities may be described by means of simple laws of mechanics, at least from a qualitative point of view. A further interesting result is that, although clearly discrete blocks were simulated, the overall behavior of the assembly is in rather good agreement with theories based on the continuum approach.

Acknowledgements

Dr. E. Gerolymatou und Prof. T. Triantafyllidis would like to acknowledge the financial support of the Marie Curie Intra-European Fellowship Programme HySM (PIEF-GA-2011-299097). Dr. S.A. Galindo Torres would like to acknowledge the support of the ARC Discovery project (DP140100490) “Qualitative and quantitative modelling of hydraulic fracturing of brittle materials”.

References

- [1] K. Hayashi, J. Willis-Richards, J. Hopkirk, Y. Niibori, Numerical models of HDR geothermal reservoirs: a review of current thinking and progress, *Geothermics* 28 (1999) 507–518.
- [2] T. Kohl, T. Mégel, Predictive modeling of reservoir response to hydraulic stimulations at the European International Journal of Rock Mechanics and Mining Sciences 44 (8) (2007) 1118–1131. doi:10.1016/j.ijrmms.2007.07.022. URL <http://linkinghub.elsevier.com/retrieve/pii/S1365160907001177>
- [3] J. Taron, D. Elsworth, K.-B. Min, Numerical simulation of thermal-hydrologic-mechanical-chemical processes International Journal of Rock Mechanics and Mining Sciences 46 (5) (2009) 842–854. doi:10.1016/j.ijrmms.2009.01.008. URL <http://linkinghub.elsevier.com/retrieve/pii/S1365160909000215>
- [4] T. Bai, L. Maerten, M. Gross, A. Aydin, Orthogonal cross joints: do they imply a regional stress rotation?, *Journal of Structural Geology* 24 (2002) 77–88.
- [5] J. Suppe, Principles of structural geology, Prentice-Hall, 1985.
- [6] K.-I. Eshiet, Y. Sheng, J. Ye, Microscopic modelling of the hydraulic fracturing process, *Environmental Earth Sciences* 68 (4) (2013) 1169–1186. doi:10.1007/s12665-012-1818-5.
- [7] A. Al-Busaidi, J. Hazzard, R. Young, Distinct element modeling of hydraulically fractured lac du bonnet granite, *Journal of Geophysical Research: Solid Earth* 110 (2005) B06302. doi:10.1029/2004JB003297.
- [8] M. Sousani, K.-I. Eshiet, D. Ingham, M. Pourkashanian, Y. Sheng, Modelling of hydraulic fracturing process by coupled discrete element and fluid dynamic methods, *Environmental Earth Sciences* available online (2014) 1–17. doi:10.1007/s12665-014-3244-3.

- [9] F. Cappa, Y. Guglielmi, V. Soukatchoff, J. Mudry, C. Bertrand, A. Char-
moille, Hydromechanical modeling of a large moving rock slope inferred
420 from slope levelling coupled to spring long-term hydrochemical monitoring:
example of the La Clapière landslide (Southern Alps, France), *Journal of
Hydrology* 291 (1-2) (2004) 67–90.
- [10] A. Riahi, Discrete element modeling of thermo-hydro-mechanical cou-
pling in enhanced geothermal reservoirs, in: *Thirty-Eighth Workshop on
425 Geothermal Reservoir Engineering*, Stanford University, California, 2014,
pp. 1–9.
- [11] F. Hamidi, A. Mortazavi, A new three dimensional approach to numeri-
cally model hydraulic fracturing process, *Journal of Petroleum Science and
Engineering* 124 (2014) 451–467.
- 430 [12] P. Fu, S. Johnson, C. Carrigan, An explicitly coupled hydro-geomechanical model for simulating hydra-
International Journal for Numerical and Analytical Methods in Geome-
chanics 37 (14) (2013) 2278–2300. doi:10.1002/nag.2135.
URL <http://dx.doi.org/10.1002/nag.2135>
- [13] G. Grasselli, A. Lisjak, O. Mahabadi, B. Tatone, Influence of pre-existing
435 discontinuities and bedding planes on hydraulic fracturing initiation, *Eu-
ropean Journal of Environmental and Civil Engineering* In press (0) (2014)
1–18.
- [14] S. Galindo-Torres, J. Muñoz-Castaño, Simulation of the hydraulic fracture
process in two dimensions using a discrete element method, *Physical Review
440 E* 75 (2007) 066109.
- [15] S. Galindo-Torres, MechSys Programming Library, [http://mechsys.
nongnu.org/index.shtml](http://mechsys.nongnu.org/index.shtml), 2014.
- [16] S. Galindo-Torres, F. Alonso-Marroquín, Y. Wang, D. Pedroso,
J. Muñoz Castaño, Molecular dynamics simulation of complex particles

- 445 in three dimensions and the study of friction due to nonconvexity, *Physical Review E* 79 (2009) 60301.
- [17] S. Galindo-Torres, D. Pedroso, Molecular dynamics simulations of complex-shaped particles using voronoi-based spheropolyhedra, *Physical Review E* 81 (6) (2010) 061303.
- 450 [18] S. Galindo-Torres, A coupled Discrete Element Lattice Boltzmann method for the simulation of fluid–solid interaction with particles of general shapes, *Computer Methods in Applied Mechanics and Engineering* 265 (2013) 107–119.
- [19] S. Behraftar, S. Galindo Torres, A. Scheuermann, D. Williams, E. Marques, H. Janjanid, Validation of a novel discrete-based model for fracturing of brittle materials, *International Journal of Rock Mechanics & Mining Sciences* (submitted) (2015) 1–14.
- 455 [20] P. Cundall, O. Strack, A discrete numerical model for granular assemblies, *Géotechnique* 29 (1979) 47–65.
- [21] S. Luding, Cohesive, frictional powders: contact models for tension, *Granular Matter* 10 (2008) 235–246.
- 460 [22] F. Kun, H. Herrmann, A study of fragmentation processes using a discrete element method, *Computer Methods in Applied Mechanics and Engineering* 138 (1996) 3–18.
- 465 [23] F. Kun, H. Herrmann, Transition from damage to fragmentation in collision of solids, *Physical Review E* 59 (1999) 2623–2632.
- [24] F. Wittel, F. Kun, H. Herrmann, B. Kroplin, Fragmentation of shells, *Physical Review Letters* 93 (2004) 35504–35504.
- [25] S. Galindo-Torres, D. Pedroso, D. Williams, L. Li, Breaking processes in three-dimensional bonded granular materials with general shapes, *Computer Physics Communications* 183 (2012) 266–277.
- 470

doi:10.1016/j.cpc.2011.10.001.

URL <http://www.sciencedirect.com/science/article/pii/S0010465511003298>

- 475 [26] A. Gérard, A. Genter, T. Kohl, P. Lutz, P. Rose, F. Rummel, The deep
EGS (Enhanced Geothermal System) project at Soultz-sous-Forêts (Alsace,
France), *Geothermics* 35 (2006) 473–483.
- [27] B. Valley, K. Evans, Stress state at Soultz-sous-Forêts to 5 km depth from
wellbore failure and hydraulic observations, in: *Thirty-Second Workshop
on Geothermal Reservoir Engineering*, Stanford University, Stanford, Cal-
480 ifornia, 2007, pp. SGP–TR–183.
- [28] E. Finnemore, J. Franzini, *Fluid Mechanics With Engineering Applications*,
McGraw-Hill Science, 2002.
- [29] M. McClure, R. Horne, Is pure shear stimulation always the mechanism of
stimulation in EGS?, in: *Thirty-Second Workshop on Geothermal Reser-
485 voir Engineering*, Stanford University, Stanford, California, 2013, pp. SGP–
TR–198.